INSTITUTE OF PHYSICS PUBLISHING JOURNAL OF PHYSICS B: ATOMIC, MOLECULAR AND OPTICAL PHYSICS

J. Phys. B: At. Mol. Opt. Phys. **39** (2006) 4825–4852 doi:10.1088/0953-4075/39/23/003

Dielectronic recombination of Fe^{13+}: benchmarking the M-shell

N R Badnell

Department of Physics, University of Strathclyde, Glasgow, G4 0NG, UK

Received 18 July 2006
Published 10 November 2006
Online at stacks.iop.org/JPhysB/39/4825

Abstract

We have carried-out a series of multi-configuration Breit–Pauli AUTOSTRUCTURE calculations for the dielectronic recombination of Fe^{13+}. We present a detailed comparison of the results with the high-energy-resolution measurements reported recently from the Heidelberg heavy-ion Test Storage Ring by Schmidt *et al*. Many Rydberg series contribute significantly from this initial $3s^2 3p$ M-shell ion, resulting in a complex recombination 'spectrum'. While there is much close agreement between theory and experiment, differences of typically 50% in the summed resonance strengths over 0.1–10 eV result in the experimentally based total Maxwellian recombination rate coefficient being a factor of 1.52–1.38 larger than theory over 10^4–10^5 K, which is a typical temperature range of peak abundance for Fe^{13+} in a photoionized plasma. Nevertheless, the present theoretical recombination rate coefficient is an order of magnitude larger than that used by modellers to date. This may help explain the discrepancy between the iron M-shell ionization balance predicted by photoionization modelling codes, such as ION and CLOUDY, and that deduced from the iron M-shell unresolved-transition-array absorption feature observed in the x-ray spectrum of many active galactic nuclei. Similar data are required for Fe^{8+} through Fe^{12+} in order to remove the question mark hanging over the atomic data though.

(Some figures in this article are in colour only in the electronic version)

1. Introduction

Dielectronic recombination (Burgess 1964) is the dominant electron–ion recombination process in both photoionized and electron-collisional plasmas. Extensive theoretical data are available for all K- and L-shell ions of all elements up to Zn, and selected heavy elements beyond, following the work of Badnell *et al* (2003), and are available online[1]. These data, including radiative recombination (RR), have been used to provide new ionization balances for both electron-collisional (Bryans *et al* 2006) and photoionized plasmas (Ferland 2006).

[1] Webpage http://amdpp.phys.strath.ac.uk/tamoc/DATA.

Extensive benchmarking has taken place against experiment for both low-Z (C, N, O) and higher-Z (Fe, Ni) elements—see e.g. Fogle *et al* (2005) and Savin *et al* (2006), and references therein. Work on the M-shell is sparse (beyond the simple Na-like sequence, Linkemann *et al* (1995), Fogle *et al* (2003)). Yet, M-shell Fe ions are ubiquitous in astrophysics.

It has become clear recently that dielectronic recombination (DR) rate coefficients for Fe $3p^q$ ($q = 1$–6) ions (Fe^{8+}–Fe^{13+}) are highly questionable at temperatures where these ions form in photoionized plasmas (10^4–10^5 K, say, Kallman and Bautista (2001)). This stems from the inability of photoionized plasma modelling codes, such as ION (Netzer 2004) and CLOUDY (Kraemer *et al* 2004), to model the iron M-shell unresolved-transition-array absorption feature observed in the x-ray spectrum of many active galactic nuclei. The situation can be improved by changing the ionization balance for these Fe ions at such temperatures, as first suggested by Netzer *et al* (2003), and which is achieved by increasing the dielectronic recombination rate coefficients by large factors (e.g., 2–4).

That this is a plausible approach has been verified experimentally for Fe^{13+} by Schmidt *et al* (2006) who carried-out high-energy-resolution DR measurements at the Heidelberg heavy-ion Test Storage Ring (TSR). They deduced a Maxwellian recombination rate coefficient which is up to an order of magnitude larger than that recommended by Arnaud and Raymond (1992), and (again) by Mazzotta *et al* (1998), at photoionized plasma temperatures. The latter is currently used to determine the ionization balance of iron in ION and CLOUDY, as well as in other photoionized plasma modelling codes such as XSTAR (Kallman and Bautista 2001). The reason for this difference is that the existing (recommended) theoretical dielectronic recombination contribution (Jacobs *et al* 1977) to the total recombination rate coefficient falls-off exponentially below $\sim$10 eV and the total is dominated by direct radiative recombination. A similar problem was noted by Müller (1999) for Fe^{15+} and it is prevalent also for L-shell ions, following the pioneering work of Savin *et al* (1997).

The approach of Jacobs *et al* (1977) is based upon the 'no-coupling' scheme, allows only for dipole core-excitations in the dielectronic capture process and pays no detailed attention to the positioning of near-threshold resonances. It should be noted that the work of Jacobs *et al* (1977) was motivated by applications to high-temperature electron-collision-dominated plasmas and, for such, their approach is quite reasonable.

Since then, Nahar (2000) has carried-out LS-coupling R-matrix photoionization calculations for several Si-like ions, including Fe^{12+}, and presented total (DR+RR) rate coefficients for the corresponding Fe^{13+} ion. Such an approach can be expected to include a contribution from low-lying dielectronic resonances. However, even at electron-collisional plasma temperatures, her total recombination rate coefficients are a factor of 3–4 smaller than those (for DR+RR) recommended by Arnaud and Raymond (1992).

Thus, it is clear that the DR of Fe^{13+} needs to be re-examined, especially for application to photoionized plasmas. Such a re-examination, including a comparison with the results of the measurements by Schmidt *et al* (2006), will provide a benchmark for other Fe $3p^q$ ($q =$ 2–6) ions, and the M-shell more generally.

The outline of the rest of this paper is as follows: in section 2 we describe our theoretical approach; in section 3 we make a detailed study of the structure of Fe^{13+}; in section 4 we compare our velocity-convoluted DR cross sections with those from the experiment by Schmidt *et al* (2006); and in section 5 we compare various Maxwellian recombination rate coefficients.

2. Theory

We have used AUTOSTRUCTURE (Badnell 1987, 1997) to carry-out a series of multi-configuration Breit–Pauli calculations of dielectronic recombination cross sections and rate coefficients. The

method implemented within AUTOSTRUCTURE is the independent processes, isolated resonances using distorted waves (IPIRDW) approach to DR. A detailed discussion of the validity of this approach is given by Pindzola *et al* 1992) while its advantages from a (collisional–radiative) modelling perspective are discussed by Badnell *et al* (2003).

2.1. The IPIRDW approach

Let $\sigma^j_{f\nu}(E)$ denote the partial dielectronic recombination cross section, as a function of centre-of-mass energy E, from an initial metastable state ν of an ion X^{+z}, through an autoionizing state j, into a resolved final state f of an ion X^{+z-1}. Then

$$\sigma^j_{f\nu}(E) = \hat{\sigma}^j_{f\nu} L^j(E), \tag{1}$$

where $L^j(E)$ is the Lorentzian line-shape of the resonance with energy E_j and width Γ_j (in the units of energy) given by (when energy-normalized to unity)

$$L^j(E) = \frac{\Gamma_j/(2\pi)}{(E - E_j)^2 + \Gamma_j^2/4}. \tag{2}$$

Here, $\hat{\sigma}$ denotes the integrated (partial) dielectronic recombination cross section, which is given by

$$\hat{\sigma}^j_{f\nu}(E_c) = \frac{(2\pi a_0 I_H)^2}{E_c} \frac{\omega_j}{2\omega_\nu} \frac{\tau_0 \sum_l A^a_{j\to\nu,E_c l} A^r_{j\to f}}{\sum_h A^r_{j\to h} + \sum_{m,l} A^a_{j\to m,E_c l}}, \tag{3}$$

where ω_j is the statistical weight of the $(N+1)$-electron doubly-excited resonance state j, ω_ν is the statistical weight of the N-electron target state (so, $z = Z - N$, where Z is the nuclear charge) and the autoionization (A^a) and radiative (A^r) rates are in inverse seconds. Here, E_c is the energy of the continuum electron (with orbital angular momentum l), which is fixed by the position of the resonance j relative to the continuum ν, I_H is the ionization potential energy of the hydrogen atom (both in the same units of energy) and $(2\pi a_0)^2\tau_0 = 2.6741 \times 10^{-32}$ cm^2 s.

A powerful aspect of the IPIRDW approach is that the use of equation (1) enables an analytic integration over the resonance profiles to be carried-out. This is in contrast to an R-matrix calculation which must map-out the detailed resonance structure numerically. This in itself is more demanding for DR than for electron-impact excitation since a much finer energy mesh is needed to map-out all resonances which contribute significantly to the cross section—see Gorczyca *et al* (2002) for a detailed study and discussion of the issue.

So, let $\bar{\sigma}^j_{f\nu}$ denote the corresponding energy-averaged (partial) dielectronic recombination cross section, then

$$\bar{\sigma}^j_{f\nu}(E_c) \equiv \frac{1}{\Delta E} \int_{E_c-\Delta E/2}^{E_c+\Delta E/2} \sigma^j_{f\nu}(E')\,\mathrm{d}E'. \tag{4}$$

Here, ΔE denotes the bin width energy, which is chosen so as to be large compared to the resonance width and small compared to the characteristic width of any subsequent convolution; otherwise, the choice of ΔE is arbitrary and it is usually taken to be a constant. Then,

$$\bar{\sigma}^j_{f\nu}(E_c) = \frac{1}{\Delta E} \hat{\sigma}^j_{f\nu}(E_c). \tag{5}$$

Thus, for a fixed j and ν, the energy-averaged partial DR cross section takes-on a nonzero value at a single energy, E_c, including when summed-over final states f. Most applications involve a sum over resonance levels j and it is convenient to 'bin' the cross section via

$$\bar{\sigma}_\nu(E_m) = \sum_{f,j} \bar{\sigma}^j_{f\nu}(E_c) \qquad \forall \quad E_c \in [E_m, E_{m+1}), \tag{6}$$

where $E_{m+1} = E_m + \Delta E$. The sum over f is over all final states which lie below the ionization limit and which may include cascade through autoionizing levels, although a single cascade (i.e., a two-step radiative stabilization) is usually more than sufficient. For total rate coefficients, applicable to low-density plasmas, the sums over f and j are taken to convergence but for application to laboratory measurements the sum over f (and hence, in practice, j) is truncated.

2.1.1. Interference between DR and RR. This is considered in detail by Pindzola *et al* (1992). Briefly, it manifests itself in two ways. The first-order interference effect (which is inversely proportional to the Fano q-factor, or generalization there-of) arises as an asymmetry in the line-profile. This is clearly seen in photoionization experiments and R-matrix calculations, for example. Diagnostic modelling involving line-shapes must take account of this interference. But, when averaged-over the resonance line-profile, this first-order effect vanishes identically (see also Badnell and Pindzola (1992) and Behar *et al* (2000)). It is the second-order interference term (proportional to $1/q^2$) which is the leading correction to the plasma rate coefficient. This is also the reason why recombination measurements have found it almost impossible to unambiguously observe interference effects—the relative energy-spread of the merged-beams leads to an integration over resonances and so one is looking for a second-order interference effect, as opposed to the first-order one in photoionization experiments. Furthermore, since the resonance strength is typically proportional to q^2, one only obtains large (second-order) effects, i.e., small q-values, on relatively weak resonances.

2.2. Application to merged-beams measurements

Merged-beams measurements utilizing an electron-cooler determine a rate coefficient for the dielectronic recombination process. To compare with a measurement at an electron–ion centre-of-mass energy E_0, we determine a corresponding theoretical rate coefficient, $\alpha(v_0)$, formally given by

$$\alpha(v_0) = \langle v\sigma \rangle = \int \sigma(v) v f(v_0, \mathbf{v})\, \mathrm{d}\mathbf{v}, \tag{7}$$

where $f(v_0, \mathbf{v})$ is the merged-beams electron velocity distribution in the centre-of-mass frame of the ions and $v_0 = \sqrt{2E_0/m_\mathrm{e}}$, since the electrons are moving non-relativistically with mass $m_\mathrm{e} \ll m_X$, the mass of the ion X.

The experimental velocity distribution, $f(v_0, \mathbf{v})$, is a 'flattened Maxwellian' (Dittner *et al* 1986) which is characterized by two parameters, a 'parallel' temperature $T_\parallel$ and 'perpendicular' temperature $T_\perp$, with $T_\parallel \ll T_\perp$:

$$f(v_0, \mathbf{v}) = \left(\frac{m_\mathrm{e}}{2\pi k T_\parallel}\right)^{1/2} \exp\left[-\frac{m_\mathrm{e}(v_\parallel - v_0)^2}{2kT_\parallel}\right] \frac{m_\mathrm{e}}{2\pi k T_\perp} \exp\left(-\frac{m_\mathrm{e} v_\perp^2}{2kT_\perp}\right), \tag{8}$$

where $v_\parallel$ and $v_\perp$ denote the parallel and perpendicular components of $\mathbf{v}$, respectively. Note, at high energies, $E_0 \gg kT_\perp$, and $f(v_0, \mathbf{v})$ reduces to an effective Gaussian distribution with a full-width at half-maximum of $2(\ln 2 E_0 k T_\parallel)^{1/2}$.

For a bin width that is much smaller than the energy-resolution of the experiment, and on using the distribution given by equation (8), we can write equation (7) in terms of the energy-averaged cross sections and bin energies, $E_m = m_\mathrm{e} v_m^2/2$:

$$\alpha_\nu(v_0) = \sum_m \frac{\Delta E \bar{\sigma}_\nu(E_m) v_m}{2kT_\perp \sqrt{(1 - T_\parallel/T_\perp)}} \exp\left(\frac{E_0}{(kT_\perp - kT_\parallel)} - \frac{E_m}{kT_\perp}\right) [\mathrm{erf}(z_1 - z_2) + \mathrm{erf}(z_1 + z_2)], \tag{9}$$

where

$$z_1 = \left[\frac{E_m(kT_\perp - kT_\parallel)}{kT_\perp kT_\parallel}\right]^{1/2} \tag{10}$$

and

$$z_2 = \left[\frac{E_0 kT_\perp}{kT_\parallel(kT_\perp - kT_\parallel)}\right]^{1/2}. \tag{11}$$

Recall, $\bar{\sigma}_v$ has units of cm^2. Writing $v_m/2 = \sqrt{E_m/I_H}\sqrt{I_H/(2m_e)}$, we have that $\sqrt{I_H/(2m_e)} = 1.0938 \times 10^8$ cm s^{-1} is the relevant remaining constant which defines the rate coefficient.

In measurements carried-out at storage rings, the ions are circulated long enough, and the densities are low enough, for the ion population to be concentrated in the ground state, normally. In single-pass measurements, it is necessary to calculate DR cross sections for metastable levels as well and then to combine them using experimental metastable fractions, if possible, or, typically, to use fractions for which the resulting cross section best matches the measured.

2.2.1. Survival of the species. Recombined ions with high principal quantum numbers are re-ionized by the strong electric field present in the charge-state analyser which is used to separate the recombined ions from the original ion beam, and so are not counted as recombined ions. A 'hard' cut-off at n_c, given by the hydrogenic expression (Bethe and Salpeter 1957)

$$n_c = \left(6.2 \times 10^8 z^3 / F\right)^{1/4}, \tag{12}$$

where F (V cm^{-1}) is the field strength, often suffices. Sometimes, however, recombined ions with $n > n_c$ have time to radiatively stabilize to $n < n_c$ during the time-of-flight (τ_F) from the cooler to the analyser and so survive to be counted. This is modelled theoretically through the use of a 'soft' or 'delayed' cut-off (Zong *et al* 1998, Schippers *et al* 2001). A soft cut-off simply imposes a higher effective n_c based-upon the lifetime of the Rydberg states. The delayed cut-off approach determines, for $n > n_c$, the lifetime of each Rydberg state (usually hydrogenic), τ_{nl}, and multiplies each nl partial DR cross section by a survival probability, given by

$$P_{nl} = 1 - \frac{\tau_{nl}}{\tau_L}\exp\left(\frac{-\tau_F}{\tau_{nl}}\right)\left[\exp\left(\frac{\tau_L}{2\tau_{nl}}\right) - \exp\left(\frac{-\tau_L}{2\tau_{nl}}\right)\right], \tag{13}$$

where τ_L is the time-of-flight for the passage through the merged-beams section of the cooler. It is often the case that $\tau_L \ll \tau_{nl}$ for the contributing nl and so, to a good approximation,

$$P_{nl} = 1 - \exp\left(\frac{-\tau_F}{\tau_{nl}}\right), \tag{14}$$

i.e., independent of the cooler time-of-flight. The shortest lifetimes are for the lowest $n > n_c$ and lowest l since the latter can radiate ($n \to n'$) to the lowest possible n'-states. Thus, the final result is relatively insensitive to the range of $n > n_c$ considered, provided that there no other magnets resulting-in significant cut-offs.

A more elaborate, experimental set-up dependent, approach is described by Schippers *et al* (2001) which takes account of the cooler geometry and the position of the various magnets and their fields as they impinge upon the recombined ions along their path to ultimate survival to be counted as recombined, or not. In addition, field ionization rates, due to Damburg and Kolosov (1979), are calculated explicitly.

2.3. Application to Maxwellian plasmas

The usual expression for the Maxwellian partial DR rate coefficient (e.g. Badnell *et al* (2003)) can be obtained simply from the corresponding integrated DR cross section, given by equation (3):

$$\alpha^j_{f\nu}(T) = \left(\frac{4\pi a_0^2 I_{\rm H}}{kT}\right)^{3/2} \frac{E_{\rm c}}{(2\pi a_0 I_{\rm H})^2 \tau_0} \hat{\sigma}^j_{f\nu}(E_{\rm c}) \exp\left(\frac{-E_{\rm c}}{kT}\right), \tag{15}$$

where $\left(4\pi a_0^2\right)^{3/2} = 6.6011 \times 10^{-24}$ cm^3. Trivially, it can also be determined from the energy-averaged DR cross section, $\bar{\sigma}$, for $kT \gg \Delta E$, on substituting for $\hat{\sigma}$ in equation (15) from equation (5).

Total DR-plus-RR rate coefficients are required for plasma modelling. We determine the RR contribution using AUTOSTRUCTURE also, following Badnell and Seaton (2003) and Badnell (2006a).

2.3.1. Fits to totals. It is convenient often for modelling purposes to fit the total (Maxwellian) DR rate coefficient, $\alpha^{\rm DR}_\nu(T)$, to the following functional form:

$$\alpha^{\rm DR}_\nu(T) = T^{-3/2} \sum_i c_i \exp\left(\frac{-E_i}{T}\right), \tag{16}$$

where the E_i are in the units of temperature, T, (eV or K) and the units of c_i are then cm^3 s^{-1} [eV or K]$^{3/2}$.

The same is also true for RR, for which we use the usual (Verner and Ferland 1996) functional form:

$$\alpha^{\rm RR}_\nu(T) = A \left[\left(\frac{T}{T_0}\right)^{1/2} \left(1 + \left(\frac{T}{T_0}\right)^{1/2}\right)^{1-B} \left(1 + \left(\frac{T}{T_1}\right)^{1/2}\right)^{1+B}\right]^{-1}, \tag{17}$$

where T_0, T_1 are in the units of temperature (eV or K) and the units of A are cm^3 s^{-1}, while B is dimensionless. A more accurate representation (Gu 2003), especially for low-charge ions, replaces B as

$$B \rightarrow B + C \exp\left(-\frac{T_2}{T}\right), \tag{18}$$

where, again, C is dimensionless and T_2 has the units of temperature.

3. The Fe^{13+} target

The DR reactions which we take account of are defined by the N-electron target configuration interaction expansion which we use. All possible $(N + 1)$-electron configurations are then constructed by adding a continuum or bound orbital to them. All possible autoionization and (electric dipole) radiative rates are determined from these configurations, and are applied subsequently so as to determine partial and total DR cross sections, following the theory of section 2.

It is still the case, for Fe^{13+} at least, that it is convenient and meaningful to consider separately the $\Delta n = 0$ and $\Delta n = 1$ core-excitation contributions to DR since, as we shall see, our highest $n = 3$ target level lies below our lowest $n = 4$ level. Indeed, '$\Delta n = 0$' DR completely dominates over $\Delta n = 1$ at photoionized plasma temperatures, and can be expected to be the largest contribution too at collisional plasma temperatures, at least where Fe^{13+} is

normally abundant (Mazzotta *et al* 1998, Bryans *et al* 2006). This separation enables us to restrict the sum over Rydberg states to $n = 1000, l = 15$ and to $n = 100, l = 5$, for $\Delta n = 0$ and $\Delta n = 1$, respectively.

3.1. $\Delta n = 0$

We consider two different target configuration interaction expansions because carrying-out two DR calculations enables us to contrast the level of accuracy/difference in the N-electron targets with that of differences between theory and experiment for cross sections and assess the accuracy of total rate coefficients, i.e. quantify the uncertainty in the $(N + 1)$-electron problem.

We define a basis A consisting of the following configurations (assuming a closed-shell Ne-like core):

$$1 : 3s^2 3p, \quad 2 : 3s3p^2, \quad 3 : 3s^2 3d, \quad 4 : 3p^3,$$
$$5 : 3s3p3d, \quad 6 : 3p^2 3d, \quad 7 : 3s3d^2$$

and a basis B, which consists of basis A plus

$$8 : 3p3d^2.$$

Thus, $3d^3$ is the only configuration from the $n = 3$ complex which is omitted, by basis B. Configurations 1–3, plus 5, form the minimal set which allows for all ($\Delta n = 0$) one-electron promotions during the dielectronic capture process from the ground configuration. Configuration 4 mixes strongly with 5, whilst 6 and 7 (which are strongly mixed themselves) provide the leading even parity configuration interaction. Configuration 8 (basis B) provides a check on that for the odd parity.

Basis A gives rise to 37 target terms whilst basis B gives rise to 56 terms. In both cases, the radial functions were determined using the Slater-type-orbital model potential of Burgess *et al* (1989). The (3s, 3p, 3d) radial scaling parameters, λ_{nl}, were determined by minimizing the equally-weighted-sum of eigenenergies of the 18 lowest terms, which correspond to all of those which arise from the first five configurations of the basis expansions. For basis A: $\lambda_{3s} = 0.931\,73$, $\lambda_{3p} = 0.992\,55$ and $\lambda_{3d} = 0.890\,06$. For basis B: $\lambda_{3s} = 0.948\,49$, $\lambda_{3p} = 1.023\,16$ and $\lambda_{3d} = 0.868\,84$. All other radial scaling parameters were taken to be unity.

Basis A gives rise to 84 target levels whilst basis B gives rise to 129 levels. Our Breit–Pauli calculations include the one-body non-fine-structure and fine-structure operators, including the effective one-body Blume and Watson operator for the mutual-spin–orbit and spin–other-orbit interactions between valence electrons and the Ne-like closed-shells (Badnell 1997). The effect of the two-body fine-structure operators representing interactions between valence electrons (including spin–spin now) is small—of the order 10^{-4} Ry—and since they are time consuming to determine in the DR calculation we omit them, along with the two-body non-fine-structure operators which are of the same order effect.

In table 1, we compare our lowest 40 calculated level energies obtained from using bases A and B with those obtained from the NIST (2006) database and those calculated with SUPERSTRUCTURE by Storey *et al* (2000) using the Thomas–Fermi model potential. These levels are all of those which arise from the lowest five configurations, i.e., it includes all levels which contribute to $\Delta n = 0$ DR in the absence of configuration mixing. We note a distinct improvement in the agreement with the results of (basis 2 of) Storey *et al* (2000), and with the observed energies, on going from basis A to basis B. Basis 2 of Storey *et al* (2000) included all configurations from the $n = 3$ complex as well as $n = 4$ configurations of the form $3s^2 4l$ and

Table 1. Level energies (Ry) for Fe^{13+}.

Level	Config.	$(2S+1)$[a]	L	$2J$	Basis A[b]	Basis B[b]	Basis 2[c]	Observed[d]
1	1	−2	1	1	0.000 00	0.000 00	0.000 00	0.000 00
2	1	−2	1	3	0.160 12	0.158 17	0.168 50	0.171 80
3	2	4	1	1	2.010 96	2.028 37	2.027 29	2.051 39
4	2	4	1	3	2.075 65	2.092 13	2.095 68	2.121 33
5	2	4	1	5	2.159 15	2.174 64	2.182 29	2.208 79
6	2	2	2	3	2.711 44	2.727 42	2.730 82	2.726 89
7	2	2	2	5	2.728 78	2.744 44	2.749 89	2.747 19
8	2	2	0	1	3.328 05	3.339 49	3.362 57	3.323 33
9	2	2	1	1	3.549 92	3.561 80	3.583 71	3.540 36
10	2	2	1	3	3.623 33	3.635 06	3.657 13	3.613 28
11	3	2	2	3	4.369 90	4.374 79	4.386 76	4.312 33
12	3	2	2	5	4.392 02	4.397 60	4.408 89	4.330 36
13	4	−2	2	3	5.259 86	5.250 43	5.254 64	5.252 39
14	4	−2	2	5	5.288 24	5.281 26	5.287 80	5.287 47
15	4	−4	0	3	5.417 28	5.356 36	5.376 40	5.367 38
16	5	−4	3	3	5.867 40	5.87474	5.876 85	
17	4	−2	1	1	5.945 70	5.864 87	5.883 62	5.853 16
18	4	−2	1	3	5.963 95	5.890 96	5.910 09	5.881 40
19	5	−4	3	5	5.902 86	5.911 36	5.913 32	5.886 68
20	5	−4	3	7	5.954 50	5.962 89	5.9659 0	5.940 97
21	5	−4	3	9	6.025 72	6.033 78	6.038 78	6.016 76
22	5	−4	1	5	6.330 30	6.316 38	6.335 38	6.290 51
23	5	−4	2	3	6.348 70	6.332 24	6.356 18	6.312 00
24	5	−4	2	1	6.362 53	6.342 47	6.370 66	6.325 72
25	5	−4	2	7	6.448 27	6.425 79	6.456 19	6.409 79
26	5	−4	1	1	6.434 41	6.422 58	6.445 98	6.413 04
27	5	−4	2	5	6.449 13	6.428 96	6.457 59	6.416 36
28	5	−4	1	3	6.443 22	6.427 49	6.453 42	6.417 22
29	5	−2	2	3	6.674 29	6.567 24	6.592 49	6.535 56
30	5	−2	2	5	6.676 11	6.573 30	6.597 85	6.541 63
31	5	−2	3	5	6.909 10	6.862 20	6.882 92	6.788 62
32	5	−2	3	7	7.036 25	6.988 36	7.013 33	6.923 93
33	5	−2	1	3	7.495 02	7.419 84	7.469 65	7.354 95
34	5	−2	1	1	7.547 17	7.489 92	7.543 20	
35	5	−2	3	7	7.670 57	7.550 01	7.573 52	7.450 46
36	5	−2	3	5	7.694 03	7.572 86	7.598 29	7.477 87
37	5	−2	1	1	7.972 68	7.751 85	7.791 03	7.650 01
38	5	−2	2	3	7.922 98	7.748 67	7.801 63	7.661 71
39	5	−2	1	3	8.00254	7.78798	7.829 00	7.687 96
40	5	−2	2	5	7.958 56	7.776 61	7.830 24	7.695 44

[a] >0 denotes even parity, <0 odd parity.
[b] This work.
[c] Storey *et al* (2000).
[d] NIST (2006).

3s3p4l, for $l = 0$–3. We note little improvement in the agreement with the observed energies resulting from the use by Storey *et al* of their larger target basis 2, compared to basis B. Some high-lying levels (37–40) are now in observed order but, on the other hand, many of the levels of configuration 5 (3s3p3d) are distinctly higher, compared to the observed, than are those from basis B.

Nevertheless, differences of up to 0.07 Ry (mostly up to 0.03 Ry for basis B) between the calculated and observed low-lying level energies mean that it is important to use the observed target energies to position the DR resonances, so as to eliminate sensitivity to the exponential factor in equation (15) at photoionized plasma temperatures. This is done simply by moving each $(N+1)$-electron autoionizing level by the difference between the calculated and observed excitation energies between the initial and parent N-electron level energies.

Generally, $A^{\rm r} \ll A^{\rm a}$ for $\Delta n = 0$ DR and so $\hat{\sigma} \propto A^{\rm r}$ (see equation (3)). Excepting DR via the fine-structure core-excitation ($3p_{1/2}$–$3p_{3/2}$), $A^{\rm r}$ is dominated by the inner-electron (dipole) radiative rate. Thus, it is instructive to study radiative rates for Fe^{13+} in some detail. In table 2, we compare our radiative rates obtained from using bases A and B with those determined by Storey *et al* (2000) from the 'extended' basis 2 of Storey *et al* (1996). This 'extended' basis 2 includes the configurations of basis 2 (Storey *et al* 2000) but adds further configurations involving $n = 4$ orbitals. In addition, all of the $n = 4$ orbitals are now pseudo-orbitals (they were physical in the vanilla basis 2)—see Storey *et al* (1996) for further details. As far as (total) DR cross sections are concerned, the distribution of radiative rates over the final states is irrelevant, in general, so long as they are all bound. Thus, we have summed over the fine-structure levels of the lower term to make the comparison shown in table 2.

Overall, we observe no drastic difference between the results obtained on using bases A and B compared to those of Storey *et al* (2000). The results of basis B tend to be closer to those of Storey *et al* (2000), than for basis A, for the strong radiative rates ($\sim 10^{10}\,{\rm s}^{-1}$), especially from configuration 5 (3s3p3d). A general point is illustrated by the results for the spin-quartet level 16. This level mixes with the nearby doublet level 18 (both $J = 3/2$, odd parity). Consequently, rates from level 16 to lower-lying spin-doublets are very sensitive to the precise mixing. Of course, as far as DR is concerned, if the autoionization rates associated with these parents are such that $A^{\rm a} \gg A^{\rm r}$ then the DR cross section is simply redistributed from one peak to another, the parents being less than 0.5 eV apart.

3.2. $\Delta n = 1$

$\Delta n = 1$ core-excitation contributions to DR come into play at high temperatures, i.e., in electron-collision-dominated plasmas. Like the case of 1–2 core-excitations in Li-, Be- and B-like ions, we expect the contribution from 'inner-shell' 2–3 core-excitations to rapidly decrease as we progress through Na-, Mg- and Al-like due to the increasing number of core-rearrangement autoionization channels. We consider both 2–3 and 3–4 $\Delta n = 1$ core-excitations so as to get a precise assessment of their relative importance and an indication of whether, or not, 2–3 core-excitations need to be considered beyond Al-like. The $\Delta n = 1$ contribution to a Maxwell rate coefficient is not sensitive to resonance positions, and so the *ab initio* calculated energies were used throughout.

3.2.1. 3–4. Again, we used two different configuration basis sets for 3–4 core-excitations so as to gain insight into the uncertainty of the theoretical results. The first (basis C) consisted of basis A, plus $3s^24l$, $3s3p4l$, $3p^24l$, for $l = 0$–3. These 19 configurations give rise to 250 target levels. The scaling parameters for the Slater-type-orbital model potential were determined from a subset of these configurations: $3s^2nl$, for $n = 3, 4$ and all l. The reason for this is to ensure that the optimization procedure for the $n = 4$ orbitals was tightly linked to the $n = 4$ term energies. The 3p and 3d scaling parameters were determined first by minimizing on the lowest two terms. These were then fixed and the $4l$ scaling parameters determined by minimizing the equally-weighted sum of $n = 4$ term energies (still in the presence of the $n = 3$ states). The result: $\lambda_{3p} = 0.695\,56$, $\lambda_{3d} = 0.716\,07$, $\lambda_{4s} = 0.796\,59$, $\lambda_{4p} = 0.7903$,

Table 2. Radiative transition rates, $A^{\rm r}(s^{-1})$, for Fe^{13+}.

j	f	Basis A[a]	Basis B[a]	Basis 2*[b]	j	f	Basis A[a]	Basis B[a]	Basis 2*[b]
3	1−2	3.25(07)[c]	3.25(07)	3.66(07)	25	7	2.75(08)	2.53(08)	3.26(08)
4	1−2	6.07(06)	6.28(06)	6.78(06)	26	4	3.09(10)	2.97(10)	2.79(10)
5	2	2.19(07)	2.28(07)	2.65(07)	26	6	3.94(07)	3.67(07)	4.29(07)
6	1−2	2.56(09)	2.73(09)	2.46(09)	27	4−5	4.08(10)	3.92(10)	3.71(10)
7	2	2.07(09)	2.23(09)	1.91(09)	27	6−7	4.61(07)	1.27(08)	1.82(08)
8	1−2	1.95(10)	1.95(10)	1.89(10)	28	4−5	3.59(10)	3.40(10)	3.19(10)
9	1−2	3.80(10)	3.90(10)	3.43(10)	28	6−7	1.14(08)	1.41(08)	1.93(08)
10	1−2	4.36(10)	4.47(10)	4.05(10)	29	3−4	3.29(08)	4.33(08)	5.38(08)
11	1−2	4.71(10)	4.65(10)	4.36(10)	29	6−7	3.95(10)	3.54(10)	3.33(10)
12	2	4.32(10)	4.28(10)	3.97(10)	29	8	3.93(08)	2.87(08)	3.49(08)
13	3−5	4.85(08)	1.14(09)	1.24(09)	29	9−10	1.76(09)	1.49(09)	1.36(09)
13	6−7	3.27(09)	3.50(09)	2.99(09)	29	11	5.28(08)	4.82(08)	4.07(08)
13	8	3.08(08)	3.41(08)	3.80(08)	30	4−5	3.57(08)	5.30(08)	6.09(08)
13	9−10	5.97(08)	6.04(08)	5.00(08)	30	6−7	3.96(10)	3.51(10)	3.28(10)
13	11	7.11(06)	6.13(06)	6.51(06)	30	10	1.20(09)	9.72(08)	8.45(08)
14	5	7.58(07)	8.23(07)	9.50(07)	30	11−12	5.96(08)	5.21(08)	4.45(08)
14	6−7	3.46(09)	3.76(09)	3.25(09)	31	4−5	9.95(07)	8.55(08)	1.10(08)
14	10	7.02(08)	7.30(08)	6.67(08)	31	6−7	1.96(10)	1.71(10)	1.55(10)
14	12	7.47(06)	6.82(06)	7.71(06)	31	11−12	1.45(09)	1.80(09)	1.54(09)
15	3−5	4.06(10)	3.78(10)	3.41(10)	32	5	4.04(08)	3.68(08)	4.36(08)
15	6	4.54(07)	1.10(08)	1.09(08)	32	7	2.10(10)	1.81(10)	1.62(10)
15	10	5.18(07)	6.00(07)	6.45(07)	32	12	1.55(09)	2.03(09)	1.95(09)
16	3−4	9.87(07)	1.85(08)	1.53(08)	33	3	2.82(08)	2.56(08)	2.87(08)
16	6−7	1.52(08)	1.16(09)	4.53(08)	33	8	4.69(10)	4.13(10)	4.03(10)
16	8	6.11(06)	1.92(08)	5.54(07)	33	9−10	1.00(10)	1.19(10)	1.00(10)
16	9−10	4.11(07)	2.34(08)	5.75(07)	33	11−12	6.70(08)	8.76(08)	9.77(08)
16	11	1.51(06)	4.13(06)	3.24(06)	34	3	1.28(08)	1.18(08)	1.28(08)
17	3−4	3.81(07)	4.03(07)	4.17(07)	34	6	3.81(08)	9.49(07)	2.54(08)
17	6	1.44(10)	1.35(10)	1.21(10)	34	8	2.11(10)	1.60(10)	1.44(10)
17	8	1.56(08)	2.16(08)	9.18(07)	34	9−10	3.02(10)	3.30(10)	3.09(10)
17	9−10	4.19(09)	4.47(09)	3.90(09)	34	11	1.13(09)	1.01(08)	2.80(08)
18	3−5	7.87(08)	6.98(08)	8.37(08)	35	5	2.80(08)	2.60(08)	3.23(08)
18	6−7	1.29(10)	1.10(10)	1.04(10)	35	7	2.84(10)	2.90(10)	2.81(10)
18	8	1.84(09)	1.90(09)	1.69(09)	35	12	2.98(10)	2.61(10)	2.22(10)
18	10	2.85(09)	2.80(09)	2.56(09)	36	6−7	2.97(10)	2.98(10)	2.87(10)
19	4−5	2.06(08)	2.21(08)	2.48(08)	36	10	2.61(08)	4.70(08)	3.76(08)
19	6−7	5.98(07)	7.70(07)	8.57(07)	36	11−12	3.10(10)	2.73(10)	2.24(10)
19	10	6.38(05)	6.57(05)	5.65(05)	37	8	1.43(10)	1.78(10)	1.57(10)
19	11	3.42(06)	4.22(06)	4.99(06)	37	9−10	3.22(10)	1.98(10)	1.98(10)
20	5	2.38(08)	2.57(08)	2.94(08)	37	11	3.66(10)	3.26(10)	2.75(10)
20	7	5.21(05)	5.28(05)	1.06(06)	38	6−7	2.67(08)	2.38(08)	2.78(08)
20	12	4.24(06)	5.05(06)	6.25(06)	38	8	3.20(09)	1.11(09)	8.17(07)
22	4−5	3.05(10)	3.00(10)	2.82(10)	38	9−10	6.41(10)	5.92(10)	4.53(10)
22	6−7	4.68(08)	9.44(08)	1.13(09)	38	11−12	2.56(10)	2.15(10)	2.21(10)
22	10	2.35(07)	3.30(07)	3.73(07)	39	6−7	4.02(08)	4.76(08)	4.65(08)
22	12	1.71(07)	2.73(07)	3.00(07)	39	8	2.65(09)	6.13(09)	6.13(09)
23	3−5	3.74(10)	3.74(10)	3.55(10)	39	9−10	3.99(10)	2.82(10)	3.56(10)
23	6	2.48(08)	3.86(08)	5.04(08)	39	11−12	3.85(10)	3.39(10)	2.65(10)
24	3−4	4.40(10)	4.35(10)	4.05(10)	40	10	7.07(10)	6.25(10)	5.81(10)
25	5	4.43(10)	4.29(10)	4.04(10)	40	11−12	2.42(10)	2.13(10)	1.95(10)

[a] This work.
[b] Extended basis 2, Storey *et al* (2000).
[c] 3.25(07) denotes 3.25×10^7.

$\lambda_{4d} = 0.7821$ and $\lambda_{4f} = 0.8563$. The 3s parameter is not well determined by such a procedure, on the other hand, opening-up the 3s sub-shell would not be consistent with the procedure for the other orbitals. Hence, we simply set $\lambda_{3s} = 0.7$ for consistency with the other scaling parameters. Such a procedure is optimal for $3p \rightarrow 4l$ promotions, which can be expected to dominate the 3–4 core-excitations.

Table 3. Some $n = 4$ level energies (Ry) for Fe^{13+}, relative to the ground level.

Config.	$(2S+1)$[a]	L	$2J$	Basis C[b]	Basis D[c]	Observed[d]
4s	2	0	1	12.9023	13.2113	13.0769
4p	−2	1	1	13.9497	14.2595	14.2963
4p	−2	1	3	14.0114	14.3204	14.3434
4d	2	2	3	15.3886	15.6841	15.4549
4d	2	2	5	15.4007	15.6965	15.4668
4f	−2	3	5	16.2484	16.5705	16.2969
4f	−2	3	7	16.2518	16.5738	16.2993

[a] >0 denotes even parity, <0 odd parity.
[b] This work.
[c] Recalculated from Storey *et al* (1996).
[d] NIST (2006).

Table 4. Symmetric oscillator strengths (gf) for Fe^{13+}.

	Basis C[b]		Basis D[c]	
Transition	Length	Velocity	Length	Velocity
3p–4s	0.2043	0.2963	0.3707	0.3757
3p–4d	0.9886	1.3858	1.5037	1.5432
3d–4p	0.1766	0.2492	0.2670	0.2493
3d–4f	6.0729	7.3666	7.4848	7.2178

[b] This work.
[c] Recalculated from Storey *et al* (1996).

The second basis that we use (basis D) is the scattering target basis used by Storey *et al* (1996) for the electron-impact excitation of Fe^{13+}. It includes all configurations belonging to the $n = 3$ complex, plus $3s^2 4l$, $3s3p4l$, for $l = 0$–3. Thus, it includes the $3p3d^2$ and $3d^3$ configurations omitted by basis C but excludes the $3p^2 4l$ configurations. The focus of their work was excitation within the $n = 3$ complex, including resonances attached to $n = 4$. Resonances attached to $n = 4$ are our primary concern here. Storey *et al* (1996) used nl-dependent Thomas–Fermi model potentials, and the relevant values of the scaling parameters are listed in their table 1. There are 227 levels associated with this 17 configuration basis.

In table 3, we compare energies for the $n = 4$ levels which result from the dominant $3p \rightarrow 4l$ promotions. We note that the $3p \rightarrow 4d, 4f$ excitation energies are better represented by basis C, while basis D is somewhat better for the lower l. In table 4, we compare symmetric oscillator strengths for the $3l$–$4l'$ array, we use the LS-coupling values for simplicity. We note 20–30% differences between the results for the two bases—nearly a factor of 2 for 3p–4s. There is also much closer agreement between the length and velocity results for basis D compared to basis C. Thus, it is of interest to see how this translates into differences in the DR cross sections. These differences affect not only the radiative stabilization rates but also the (dipole) dielectronic capture and autoionization rates, including autoionization into excited states.

3.2.2. 2–3. We considered $2p \rightarrow 3l$ promotions only. The contribution from $2s \rightarrow 3l$ is <5% of the 2p by Ne-like ions. We used a target basis which comprised the first five configurations of basis A, plus $2p^5 3s^2 3p^2$, $2p^5 3s^2 3p3d$ and $2p^5 3s3p^3$; the latter so as to allow

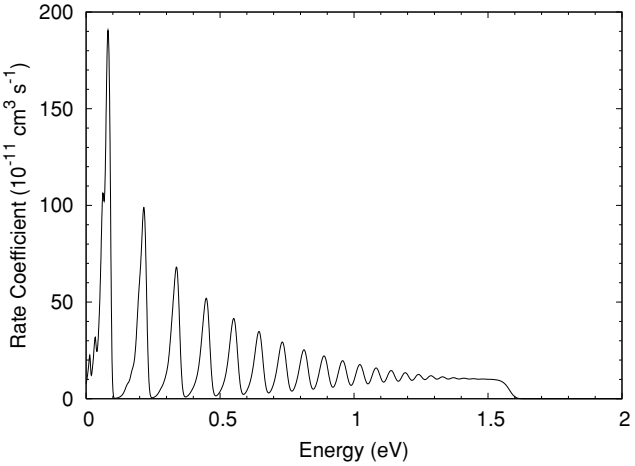

Figure 1. Velocity-convoluted DR cross sections for the fine-structure core-excitation in the ground term of Fe^{13+}.

for the strong configuration mixing with the prior. These configurations give rise to 178 target levels. In addition, we now need to allow for core-rearrangement autoionization transitions of the form: $2p^5 3l^4 nl' \rightarrow 2p^6 3l^2 nl' + e^-$, i.e., where the Rydberg electron is a spectator. These transitions strongly suppress DR since they are 'additional' autoionization pathways (those which have no reverse dielectronic capture process to balance them) and are independent of n, while the populating dielectronic capture rate scales as n^{-3}.

4. Velocity-convoluted DR cross section results

In order to make a comparison between our theoretical DR cross sections and those measured by Schmidt *et al* (2006) at TSR, we convolute them according to equation (7) using the experimentally determined $kT_\perp = 1.2 \times 10^{-2}$ eV and $kT_\parallel = 9.0 \times 10^{-5}$ eV, and initially apply a hard cut-off (see equation (12)) at $n_c = 45$.[2] It is assumed that there is no significant metastable fraction in the ion beam when it comes to the comparison with experiment, and so we consider only DR from the ground level of Fe^{13+}.

4.1. Parental contributions

Since many Rydberg series contribute to the final observed 'spectrum', we first show results for various core-excitations, labelled according to parent level (see table 1) or configuration. We also compare results obtained using target bases A and B. Note the caveat, parentage is not a good quantum number.

In figure 1, we show the convoluted theoretical DR results, which have the dimension of a rate coefficient, for the fine-structure core-excitation, i.e., parent level 1 to parent level 2, as listed in table 1. This opens-up at $n = 32$ and falls-off rapidly in n, as radiative stabilization takes place via an outer-electron transition $n \rightarrow n'$, for $n' < 32$, and which is dominated by $n' < 10$. The results from bases A and B are indistinguishable in the figure.

In figure 2, we illustrate the complexity which arises from the $3s \rightarrow 3p$ core-excitation to parent configuration 2. The lowest spectrum is the sum of contributions from the ^4P_J, ^2D_J, ^2S_J

[2] The value of $n_c = 55$ given by Schmidt *et al* (2006) is incorrect (Schmidt, private communication).

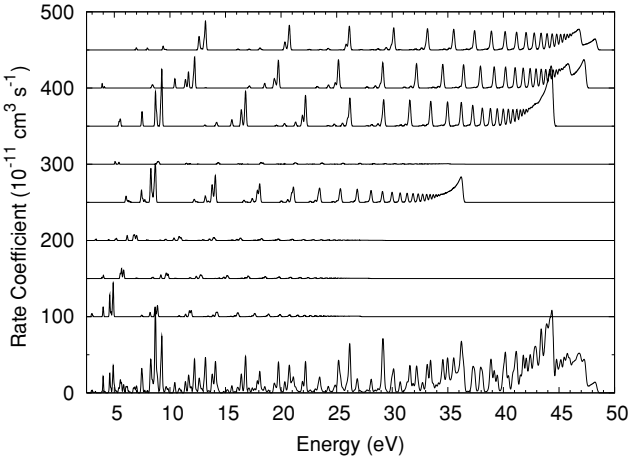

Figure 2. Velocity-convoluted DR cross sections for the 3s $\rightarrow$ 3p core-excitation to parent configuration 2. Bottom curve, summed-over all parent levels, $i = 3$–10. Offset by $1 \times 10^{-9} + (i - 3)5 \times 10^{-10}$, the contributions from the individual parent levels, i.

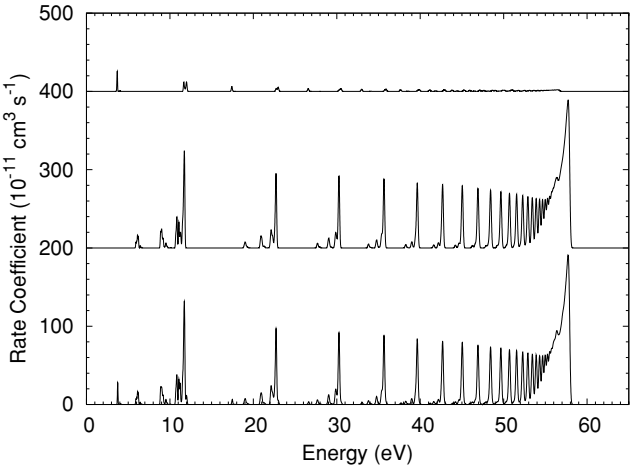

Figure 3. Velocity-convoluted DR cross sections for the 3p $\rightarrow$ 3d core-excitation to parent configuration 3. Bottom curve, summed-over all parent levels, $i = 11-12$. Offset by $(i - 10)2 \times 10^{-9}$, the contributions from the individual parent levels, i.

and ^2P_J levels. Offset above are the individual parent level, i, contributions for $i = 3$–10. The results from bases A and B are barely distinguishable in the total spectrum.

In figure 3, we present results for the 3p $\rightarrow$ 3d core-excitation. There are only two parent levels and the $^2D_{5/2}$ parent level 12 contributes only weakly as the $J = 5/2 \rightarrow 1/2$ core-radiative transition is electric-dipole-forbidden. Again, the results from bases A and B are indistinguishable in the figure.

In figure 4, we compare the results from bases A and B for excitation of the parent $3p^3$ configuration 4, summed-over all five parent levels. This excitation only takes place through configuration mixing and we note (i) that it is weak, especially above 10 eV, and (ii) that we now see some small differences between the results of bases A and B . The lowest autoionizing states have $n = 6$. Core-radiative stabilization is allowed to parent configuration

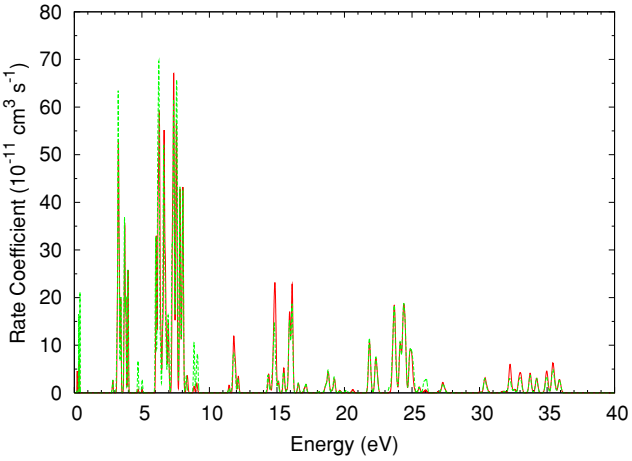

Figure 4. Velocity-convoluted DR cross sections for excitation of the parent $3p^3$ configuration. Solid (red) curve, basis A; dashed (green) curve, basis B.

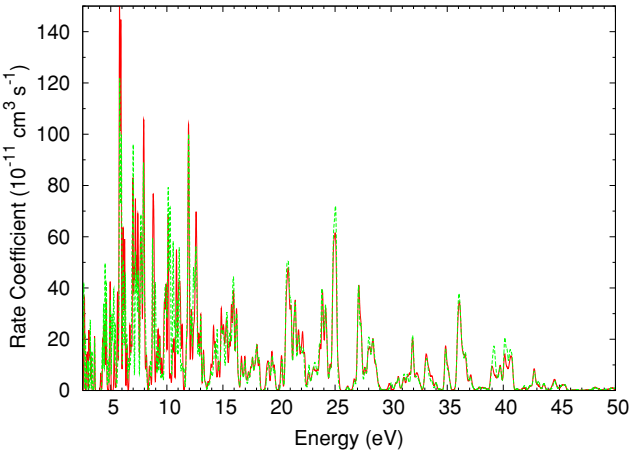

Figure 5. Velocity-convoluted DR cross sections for the 3s → 3d core-excitation of parent configuration 5. Solid (red) curve, basis A; dashed (green) curve, basis B.

2 via 3p → 3s. These 'recombined' levels then first autoionize at $n = 7$ or 8, for the spin-doublet parents.

In figure 5, we compare the results from bases A and B for the 3s → 3d core-excitation of parent configuration 5, summed-over all 23 parent levels. Again, there are small differences, below 15 eV. The lowest autoionizing states have $n = 5$ or 6, depending on the parent. There are two main core-radiative stabilization pathways: 3d → 3p, to parent configuration 2, and 3p → 3s, to parent configuration 3. These then first autoionize at $n = 7$ for the latter, and, again, between $n = 7$ and 8 for spin-doublet parents of the former. So, just a few n-values contribute strongly, but they are spread out in energy because of the 25 eV spread of levels of configuration 5.

In figures 6 to 8, we present results for core-excitations to parent configurations 6–8, which are only accessible via configuration mixing. Again, there is an allowed core-radiative-stabilization pathway for limited n-values. We see that the DR cross sections are progressively

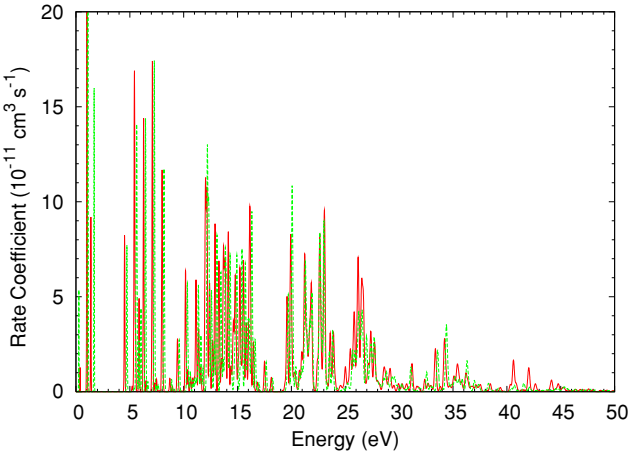

Figure 6. Velocity-convoluted DR cross sections for excitation of the parent configuration 6. Solid (red) curve, basis A; dashed (green) curve, basis B.

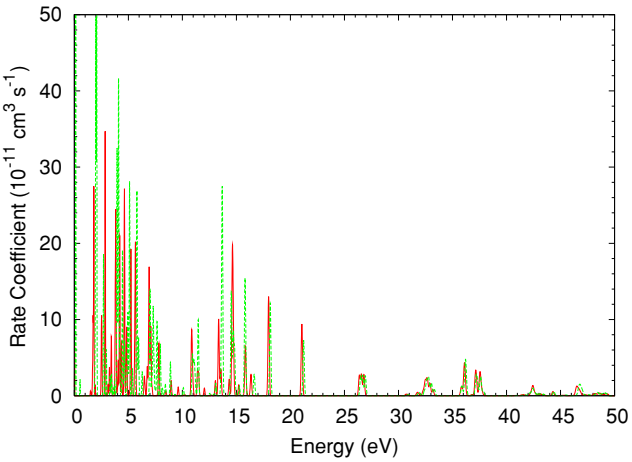

Figure 7. Velocity-convoluted DR cross sections for excitation of the parent configuration 7. Solid (red) curve, basis A; dashed (green) curve, basis B.

weaker as we go to higher-energy parent configurations. The main difference now between the results of bases A and B (see figures 6 and 7) is an energy shift, due to the fact that we only adjusted to the lowest 40 observed level energies.

We conclude that the use of observed energies mitigates against differences in the DR cross section due to the different level energies of bases A and B while differences in the radiative rates either occur for transitions which do not contribute strongly to the DR, or the rates themselves are simple redistributed amongst near-by levels.

4.2. Comparison with experiment

We consider the $\Delta n = 0$ and $\Delta n = 1$ core-excitations separately. (Low-lying resonances which arise from $n = 3$–4 capture to $n = 4$ do overlap the $\Delta n = 0$ energy range, but the peaks are so small as to be 'lost in the noise' when comparing with experiment.)

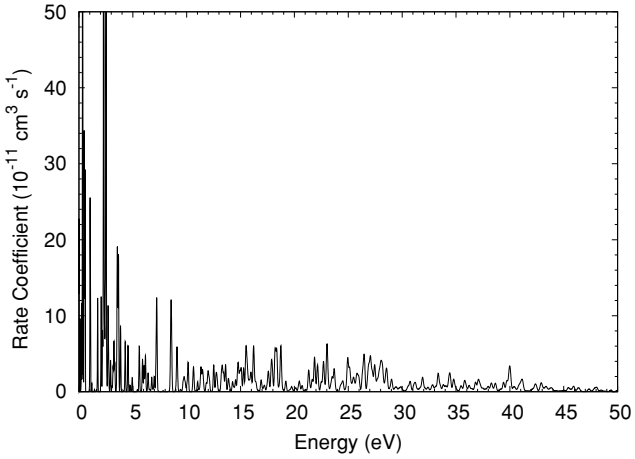

Figure 8. Velocity-convoluted DR cross sections for excitation of the parent configuration 8. Solid curve, basis B.

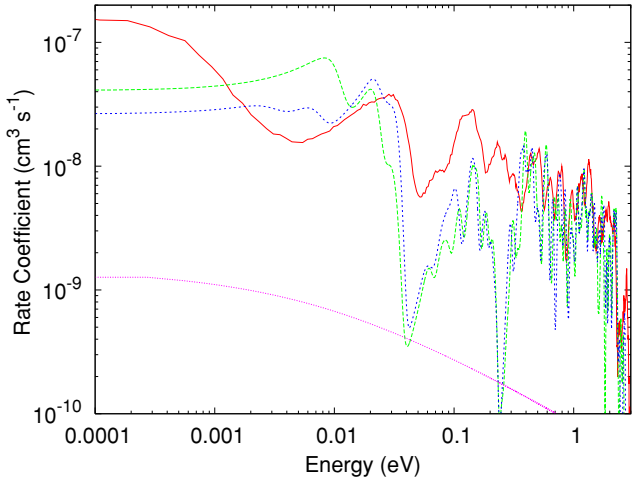

Figure 9. Velocity-convoluted recombination cross sections for Fe^{13+} near threshold. Solid (red) curve, experimental results of Schmidt *et al* (2006); long-dashed (green) curve, theoretical DR results obtained on using basis A; short-dashed (blue) curve, theoretical results obtained on using basis B; dotted (purple) curve, theoretical RR results (basis A). The theoretical results are all this work.

4.2.1. $\Delta n = 0$. In figure 9, we compare our theoretical DR results, obtained using bases A and B , with the experimental measurements of Schmidt *et al* (2006). The comparison is made very close to threshold (10^{-4}–1 eV), utilizing a log–log scale. Schmidt *et al* (2006) note a relatively small anomalous enhancement below 10^{-3} eV and so estimate the 'true' DR-plus-RR contribution to tend towards 1×10^{-7} cm^3 s^{-1} at 10^{-4} eV. The two sets of theoretical results are in accordance above ∼0.01 eV while at lower energies the results of basis B are in somewhat better agreement with experiment, down to ∼0.001 eV. Below the dip at about 0.04 eV, Schmidt *et al* show fits to 5 DR resonances. We find 14 resonances, of the form $3s^2 3p_{3/2} 32l (l = 0, 1)$, $3s3p^2\ {}^4P_{3/2}9f$ and 3s3p3d5g. Of course, our convoluted cross sections only exhibit three (basis A) or four (basis B) obvious peaks in this energy

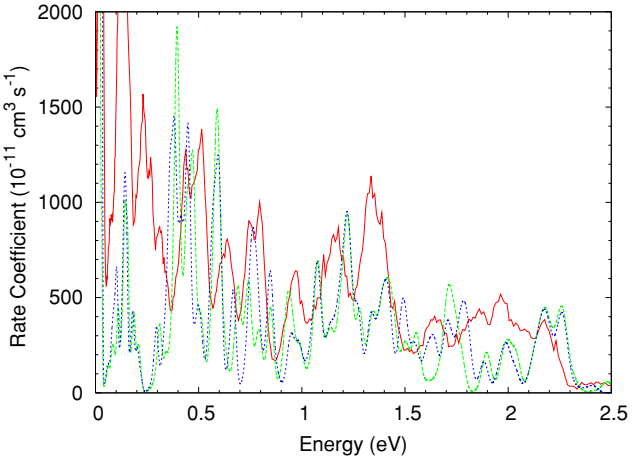

Figure 10. Velocity-convoluted $\Delta n = 0$ recombination cross sections for Fe^{13+} over 0–2.5 eV. Solid (red) curve, experimental results of Schmidt *et al* (2006); long-dashed (green) curve, theoretical DR results obtained on using basis A; short-dashed (blue) curve, theoretical results obtained on using basis B. The theoretical results are all this work.

region. We have looked at the bound-states just below threshold but they are well below the apparent uncertainties in resonance energy positioning seen in figure 9. There is substantial disagreement between theory and experiment between about 0.03 and 0.35 eV. Resonances in this region are higher members of the aforementioned series, as well as those attached to parent configurations 6 and 7. However, the differences below 0.2 eV have negligible effect on any differences in the Maxwellian rate coefficient at 2 eV. Only the differences up to 0.35 eV start to impact upon the Maxwellian rate coefficient at 2 eV. We also illustrate the RR contribution in this energy region, having applied a hard cut-off at $n_c = 45$ again.

In figure 10, we compare the results of theory and experiment near threshold again, this time using a linear plot. We see more clearly now that the theoretical results from bases A and B are in close agreement over ≈0.05–0.4 eV, but differ substantially from the measured. Overall, in this energy range, the differences between the two sets of theoretical results are not large enough to suggest an uncertainty which could account for the difference with the measured. Although, where there are more noticeable differences, the results from basis B are perhaps somewhat of an improvement over basis A. The DR cross section drops substantially (by a factor of 10, or so) above 2.34 eV because autoionization into the excited fine-structure level 2 becomes energetically allowed. This means that resonances below 2.34 eV contribute 'disproportionately' at higher temperatures—see, e.g., figure 4 of Schmidt *et al* (2006). If we sum-up the resonance strengths over 0.35 to 2.5 eV we find that the result for basis A is 3% smaller than for basis B but the measured is 33% larger.

In figure 11, we compare the results of theory and experiment over 2–10 eV. Although this is the typical temperature range of peak abundance for Fe^{13+} in a photoionized plasma, only above a temperature corresponding to about 5 eV is the Maxwellian rate coefficient dominated by the resonances above 2 eV. Again, the differences between the results of bases A and B are not too significant, but the agreement with the measured is rather poor. If we sum-up the resonance strengths over 2.5 to 10.5 eV we find that the result for basis A is 8% smaller than for basis B but the measured is 40% larger. Thus, over 2–10 eV we expect the experimentally deduced Maxwellian rate coefficient to be roughly 40% larger than the theoretical one.

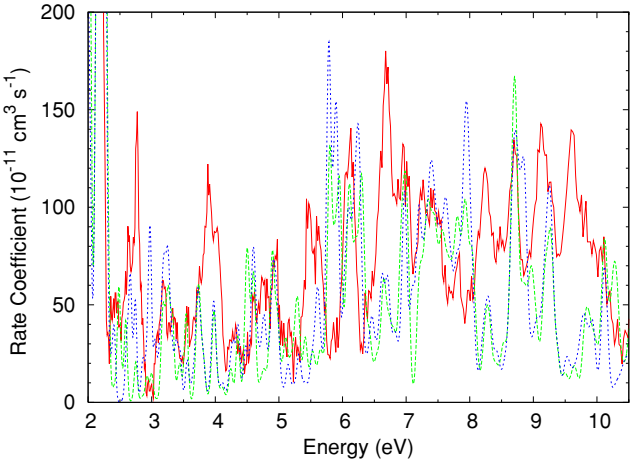

Figure 11. As figure 10, but over 2–10.5 eV.

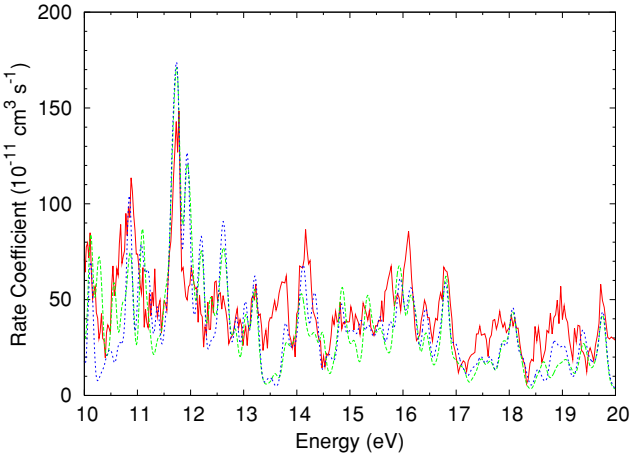

Figure 12. As figure 10, but over 10–20 eV.

In figure 12, we compare results over 10–20 eV. As we move up in energy we start to see more of a convergence between the theoretical results and the measured: the summed resonance strengths from bases A and B differ by less than 1% whilst the measured is 21% larger. However, if we now look at the energy range 20–30 eV (figure 13) we see that the measured rate coefficient appears to be sitting on a much larger 'background' over 23–29 eV—the theoretical results drop much closer to zero between the main resonance peaks, i.e., there is little 'fill-in' due to other small resonance contributions. Over 30–40 eV (figure 14) the much better agreement between theory and experiment is resumed, except over 36–37 eV. Here, there is a noticeable contribution from capture to high-n states and the comparison with experiment is dependent on (the modelling of) their survival to be detected. We illustrate with the results from two models (both for basis A) and discuss them in detail next.

In figures 15 and 16, we compare results over 40–50 eV and 50–60 eV, respectively. The resonances arise from 3s $\rightarrow$ 3p and 3p $\rightarrow$ 3d core-excitations for the former, but the second only for the latter—see figures 2 and 3. The results of bases A and B are indistinguishable on

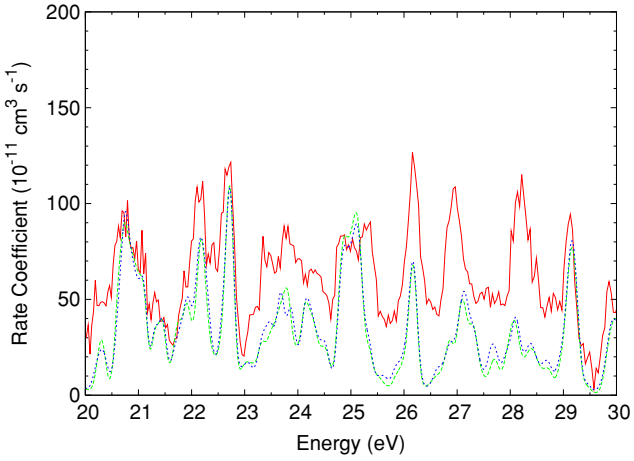

Figure 13. As figure 10, but over 20–30 eV.

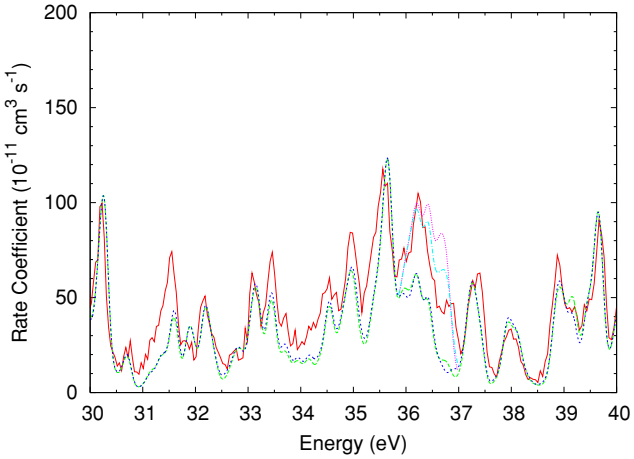

Figure 14. As figure 10, but over 30–40 eV; plus: dotted (purple) curve, delayed cut-off time-of-flight 166.5 ns; dot-dashed (light blue) curve, utilizing the survival probabilities of Schippers *et al* (2001).

this scale, and so only basis A results are shown and considered further. In these two energy regions, we address the issue of the survival of the recombined states as the ions travel from the cooler to the charge-state analyser. Recall figure 2, there are high-n DR contributions from parent levels 8–10 of configuration 2 which span 44–49 eV. (Those attached to parent level 6 affect the 36–37 eV range.) The situation, as illustrated by figure 3, is simpler for the peak at 58 eV. It is in these two energy ranges for which a hard cut-off at $n_c = 45$ results-in large discrepancies between theory and experiment. The discrepancy is reduced on implementing a delayed cut-off (equation (14)) utilizing the appropriate time-of-flight for this experiment of 166.5 ns and imposing a hard cut-off at $n_c = 95$ due to the correction magnet close to the cooler (Schippers, private communication). Further improvement in agreement is obtained on utilizing the survival probabilities of Schippers *et al* (2001), but for the DR of Fe^{13+}. These latter two sets of results are only shown at energies where they differ from the 'hard cut-off'

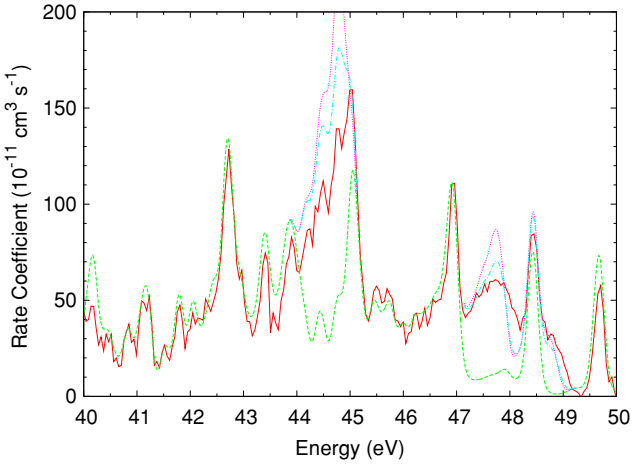

Figure 15. As figure 14, but over 40–50 eV.

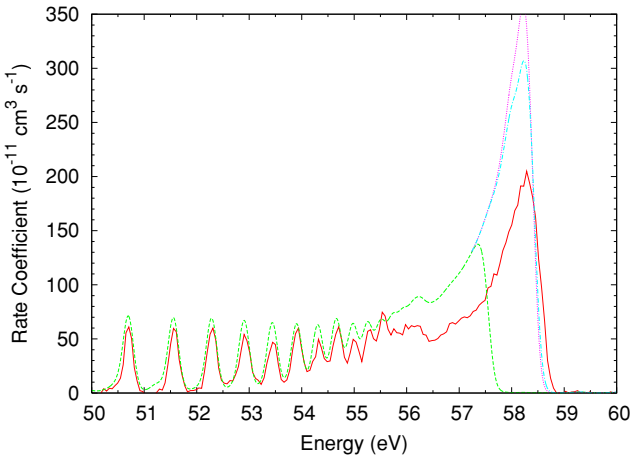

Figure 16. As figure 14, but over 50–60 eV.

results. Clearly, the final agreement between theory and experiment is sensitive to the precise contribution, i.e. survival, of recombined states with $n > 45$. While this largely accounts for the discrepancies over 44–49 eV between experiment and theory utilizing only a hard cut-off, as well as the mismatch in the final position of the Rydberg peak at 58.5 eV, it has no effect on the puzzling discrepancy between about 56 and 58 eV. Here, the experimental result actually lies at a fairly uniform 4×10^{-10} cm^3 s^{-1} below (all of) the theoretical one(s).

We close the discussion of the $\Delta n = 0$ results with a small observation: the noticeable drop in the DR cross section just below 56.5 eV (in figure 16) is due to the final-state of the $3d_{3/2} \rightarrow 3p_{3/2}$ core-radiative-stabilization pathway in fact opening-up at this point ($n = 32$) to autoionization to the $3p_{1/2}$ continuum. (We obtain 0.220 for the ratio of the $3d_{3/2} \rightarrow 3p_{3/2}$ to $3d_{3/2} \rightarrow 3p_{1/2}$ radiative rates compared to 0.225 obtained by Storey *et al* (2000)—see also table 2). Thus, there appears to be close qualitative agreement between theory and experiment for this effect. This is in stark contrast to the poor quantitative agreement for the absolute cross section.

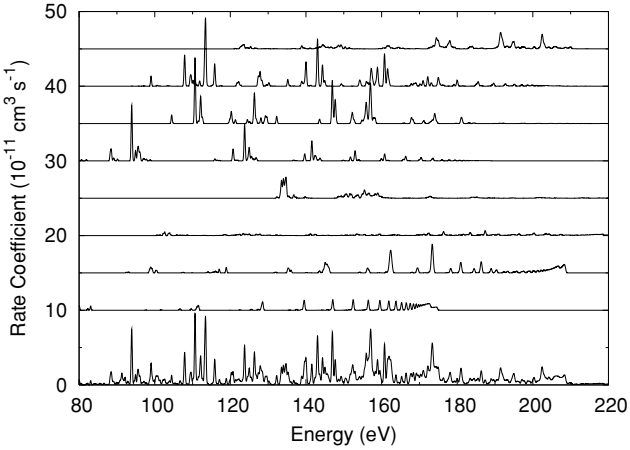

Figure 17. Velocity-convoluted DR cross sections for 3–4 core-excitations in Fe^{13+}. Bottom curve, summed-over all parent configurations. Offset (increasing) are the contributions from 3p → 4s, 4d; 3s → 4p, 4f; 3p → 4p, 4f; and 3s → 4s, 4d core-excitations.

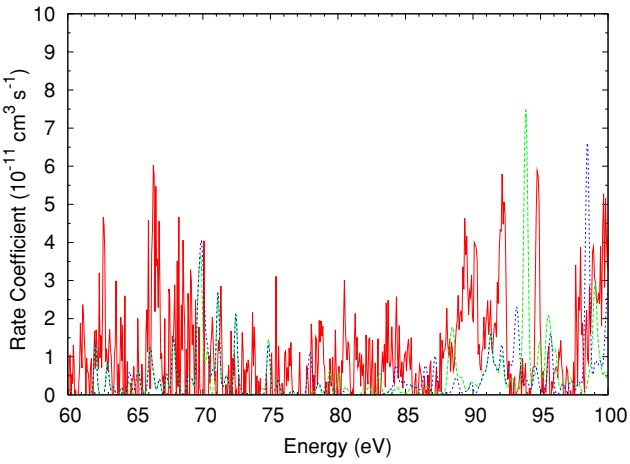

Figure 18. Velocity-convoluted $\Delta n = 1$ (3–4) DR cross sections for Fe^{13+} over 60–100 eV. Solid (red) curve, experimental results of Schmidt *et al* (2006); long-dashed (green) curve, theoretical DR results obtained on using from basis C; short-dashed (blue) curve; theoretical results from basis D. The theoretical results are all this work.

4.2.2. $\Delta n = 1$. In figure 17, we present an overview of the different contributions to the complete 3–4 'spectrum'. The first point to note is that the resonance strengths are now a factor of 10, or more, smaller than those we have seen associated with the $\Delta n = 0$ core-excitations. Only the 3p → 4s, 4d core-excitations exhibit the classic DR spectrum. The dipole core-excitations dominate, along with 3s → 4d. We see that the final total spectrum is complex, which makes it difficult to identify individual peaks in the measured spectrum.

In figures 18–21, we make comparisons between the results of our calculations with those of the experimental measurements by Schmidt *et al* (2006) for DR in the energy region in which the 3–4 core-excitations contribute.

In figure 18, it is capture to $n = 4$ which dominates, and we did not make a separate calculation using basis D since the orbitals were based on the Thomas–Fermi potential

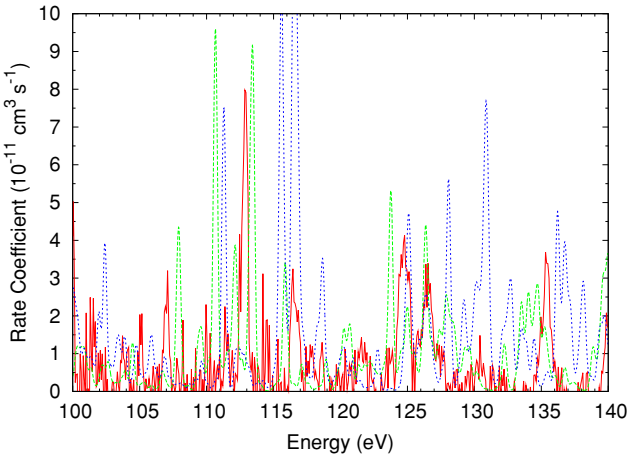

Figure 19. As figure 18, but over 100–140 eV.

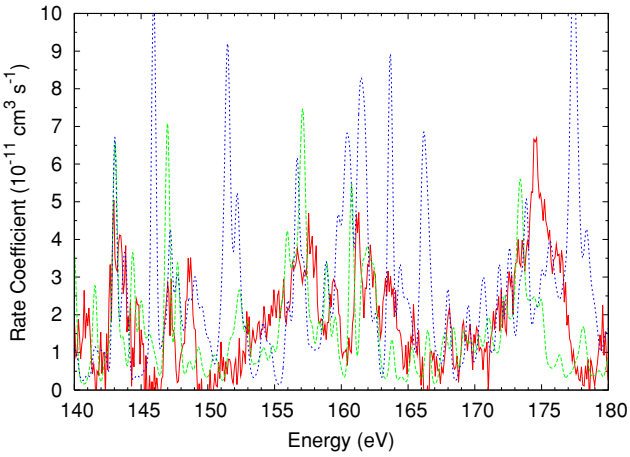

Figure 20. As figure 18, but over 140–180 eV.

optimized for the Al-like core. In the case of basis C, although we used the same scaling parameters for capture to $n = 4$ as for $n > 4$, the Slater-type-orbital model potential depends on configuration (actually, the complex) and so is inherently 'optimized' differently for capture to $n = 4$ and $n > 4$ (see Burgess *et al* (1989) for specific details). Hence, we added the basis C $n = 4$ results to those of basis D. In the 60–90 eV range, the theoretical cross sections are much weaker than the measured.

In contrast, in figures 19 and 20 we see that the theoretical DR cross sections are more strongly peaked than the measured, especially so for basis D which has the larger $4 \rightarrow 3$ radiative rates. Despite basis C apparently giving rise to a worse structure for Fe^{13+} than basis D, based upon the agreement between the length and velocity forms for the relevant oscillator strengths (see table 4), it does appear that basis C gives rise to distinctly better agreement with experiment for the DR cross sections than basis D. Although the agreement is worse than for $\Delta n = 0$ core-excitations, the sensitivity of the atomic structure to the overlap of the $n = 3$ and $n = 4$ orbitals means that the differences are 'less serious', i.e., there is still enough uncertainty in the atomic structure so that the agreement might be improved upon. We note that there is no

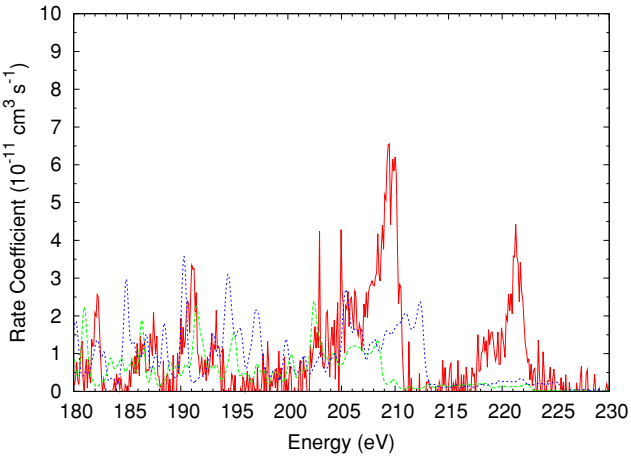

Figure 21. As figure 18, but over 180–230 eV.

simple identification of the various peaks in these figures as many different core-excitations contribute in this energy region, but they are dominated by a few low-n resonances because $\Delta n = 0$ autoionization of the final states opens-up at $n < 10$ for all parents, except $3s^2 3p$. In addition, the $3p \rightarrow 4s$ series Rydberg accumulation contributes to the peak at 175 eV.

In figure 21, we can unambiguously identify the peaks around 210 and 220 eV as being associated with the limit of the $3p \rightarrow 4d$ and $3s \rightarrow 4p$ core-excitations, but the theoretical cross sections are much smaller than measured for these peaks, especially so for the latter. The sum over n is fairly well converged by $n = 45$ and even applying no cut-off (or infinite time-of-flight) does not increase the size of the theoretical peaks by much. We do see the 'overshoot' of the basis D results here—as expected from the use of the unadjusted energies of table 3.

Summing over all DR resonance strengths for the 3–4 core-excitations we find the basis D result to be 50% larger than that for basis C, which is comparable with the excess of the 3p–(4s + 4d) oscillator strength seen in table 4. The sum of the measured DR resonance strengths in the 60–240 eV range is 21% larger than that from basis C. Of course, we have noted significant disagreements between the calculated and measured DR resonances, both over- and under-estimates.

Finally, in figure 22 we present our results for the 2–3 core-excitations. These resonances lie above the highest energy considered by Schmidt *et al* (2006). It should be noted, however, that the sum of DR resonance strengths associated with this 2–3 core-excitation is a factor of 2.5 larger than that associated with the 3–4. Thus, apart from contributing at a higher temperature, this core-excitation is likely to be more important than the 3–4 for application to collisional plasmas.

5. Maxwellian rate coefficients

In figure 23, we present our theoretical results for Maxwellian rate coefficients: RR-plus-DR from 3–3, 3–4 and 2–3 core-excitations, and compare the sum-total of these with that determined by Schmidt *et al* (2006), based primarily upon their measured DR (cooler) rate coefficients. Over 10^4–10^5 K, a typical temperature range for photoionized plasmas where Fe^{13+} is abundant, the experimentally-based total is between a factor of 1.52–1.38 larger than our theoretical total—this is inline with what we expect following our earlier detailed

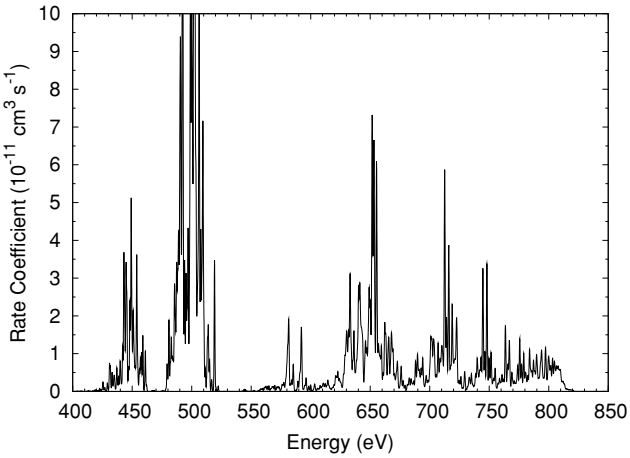

Figure 22. Velocity-convoluted $\Delta n = 1$ (2–3) recombination cross sections for Fe^{13+}. Solid curve, present theoretical results.

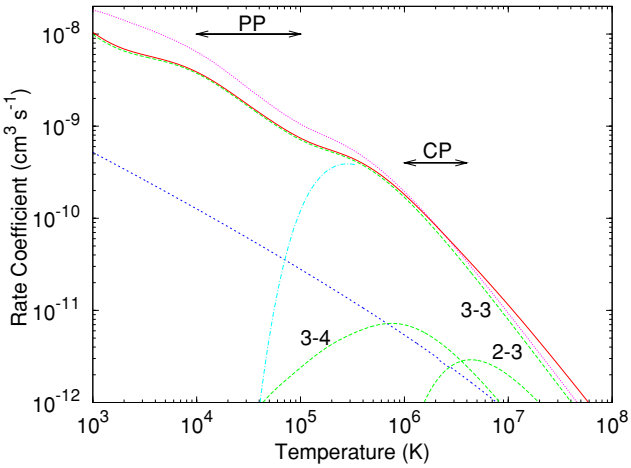

Figure 23. Maxwellian rate coefficients for Fe^{13+}. Solid (red) curve, total DR-plus-RR; short-dashed (blue) curve, RR; long-dashed (green) curves, DR for 3–3, 3–4 and 2–3 core-excitations. All this work. Dot-dashed (light blue) curve, DR of Arnaud and Raymond (1992). Dotted (purple) curve, experimentally based total of Schmidt *et al* (2006). PP and CP denote typical photoionized and electron-collisional plasma temperature ranges, respectively, for Fe^{13+} (Kallman and Bautista 2001 and Mazzotta *et al* 1998).

comparison of the DR resonances contributing at these temperatures. Nevertheless, it is clear that the total recombination rate coefficient of Fe^{13+} in photoionized plasmas is an order of magnitude larger than has been used to-date, as first pointed-out by Schmidt *et al* (2006) on the basis of their measurements for this ion. We show also only the low temperature fall-off of the recommended DR rate coefficient of Arnaud and Raymond (1992) and not any of the ad hoc changes proposed by Netzer (2004) and by Kraemer *et al* (2004).

At temperatures of a few times 10^6 K, typical of electron-collision-dominated plasmas where Fe^{13+} is abundant, the experimentally-based total is only 5% smaller than our calculated one, while the recommended data of Arnaud and Raymond (1992) lie only about 10% higher. (The data of Arnaud and Raymond (1992) are based principally upon the results of Jacobs

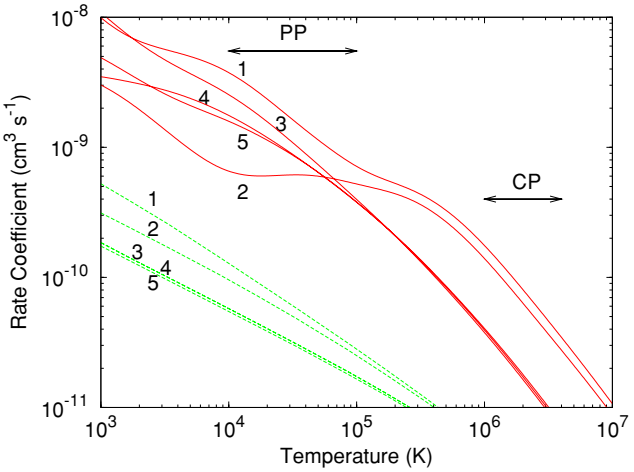

Figure 24. Total Maxwellian rate coefficients for the ground and metastable initial levels (m = 1–5) of Fe^{13+} (see text for details). Solid (red) curves, DR; dashed (green) curves, RR. All this work. PP and CP, as figure 23.

et al (1977), but include an estimate of the contribution from 2p–3d inner-shell transitions as well, which were not included by Jacobs *et al*.) We see also that both $\Delta n = 1$ contributions contribute only modestly to the total, both equally about 6% at 3×10^6 K. Far-off equilibrium, this rises to about 20% at 10^7 K with three-quarters coming from the 2–3 core-excitation. Given the modest contribution from $\Delta n = 1$ core-excitations, then, since such calculations are more demanding than for $\Delta n = 0$, the use of LS-coupling may suffice, even with the 30% difference from intermediate coupling which we note (not shown).

The LS-coupling R-matrix total recombination rate coefficients of Nahar (2000, not shown) are a factor of 3–4 smaller than the present ones across the temperature range 10^4–10^7 K, which spans all temperatures of practical interest. The discrepancy at collisional plasma temperatures is puzzling and was noted by Nahar (2000) in her comparison with the results of Jacobs *et al* (1977). Her results were not considered by Netzer (2004) or by Kraemer *et al* (2004) in their modelling.

Our rate coefficients are for the $3s^2 3p\ ^2P_{J=1/2}$ ground-level of Fe^{13+}. In photoionized plasmas, the ion population may not be concentrated in the ground level, while in electron-collisional plasmas there may be signification population of levels of the $3s3p^2\ ^4P$ term. The rate coefficients for the various metastable levels can be quite different. In figure 24, we compare and contrast total DR (i.e., summed-over all core-excitations) and RR rate coefficients from the ground and metastable levels. We index the target metastable levels by m, where $m = 1$ for the ($J = 1/2$) ground level, $m = 2$ for the other ($J = 3/2$) fine-structure level and $m = 3, 4, 5$ for the ($J = 1/2, 3/2, 5/2$) levels of the metastable term, as per table 1.

At photoionized plasma temperatures we see that the $m = 2$ metastable DR rate coefficient is an order of magnitude smaller than for the ($m = 1$) ground level—this is due primarily, of course, to the absence of the fine-structure DR pathway. The DR rate coefficients for higher metastables exhibit irregular behaviour (at low temperatures) due to the positioning close to threshold of the lowest autoionizing states, relative to these excited Fe^{13+} thresholds, although the $m = 3$ and 4 metastable levels again have fine-structure dielectronic capture pathways and the enhancement for $m = 3$ appears to be quite noticeable. At collisional-plasma temperatures, the DR rate coefficients split primarily into two groups which are based upon term, not level, as the influence of fine-structure DR and threshold effects is diminished.

Table 5. DR fitting coefficients c_i ($cm^3\ s^{-1}\ K^{3/2}$) and E_i(K) for the ground and metastable initial levels ($m = 1$–5) of Fe^{13+}.

m	c_1	c_2	c_3	c_4	c_5	c_6	c_7	c_8
1	1.090(−3)	7.801(−3)	1.132(−2)	4.740(−2)	1.990(−1)	3.379(−2)	1.140(−1)	1.250(−1)
2	3.176(−4)	1.097(−3)	1.451(−2)	4.623(−2)	1.424(−1)	3.105(−2)	1.173(−1)	1.579(−1)
3	9.230(−4)	4.787(−3)	7.598(−3)	1.538(−2)	1.512(−2)	1.711(−2)	9.083(−3)	4.875(−1)
4	6.837(−4)	3.386(−3)	8.737(−3)	2.334(−2)	2.819(−2)	1.282(−2)	9.735(−3)	2.670(−1)
5	5.606(−4)	3.306(−3)	9.372(−3)	1.635(−2)	1.674(−2)	1.783(−2)	9.195(−3)	3.689(−1)
m	E_1	E_2	E_3	E_4	E_5	E_6	E_7	E_8
1	1.246(3)	1.063(4)	4.719(4)	1.952(5)	5.637(5)	2.248(6)	7.202(6)	3.999(9)
2	1.204(3)	1.214(4)	5.689(4)	1.983(5)	5.340(5)	2.414(6)	7.302(6)	4.245(9)
3	9.887(2)	1.075(4)	4.542(4)	1.832(5)	5.506(5)	1.692(6)	6.994(6)	2.789(9)
4	1.824(3)	1.101(4)	4.775(4)	2.131(5)	1.109(6)	5.479(6)	1.365(9)	2.517(9)
5	1.288(3)	1.171(4)	4.780(4)	1.828(5)	5.530(5)	1.697(6)	6.960(6)	2.666(9)

Table 6. RR fitting coefficients for the ground and metastable initial levels ($m = 1$–5) of Fe^{13+}.

m	A ($cm^3\ s^{-1}$)	B	T_0 (K)	T_1 (K)	C	T_2 (K)
1	4.321(−10)	0.6091	2.255(03)	4.962(07)	0.0356	1.006(05)
2	2.031(−11)	0.5464	2.669(05)	5.310(07)	0.0277	9.907(08)
3	1.591(−09)	1.0274	1.196(01)	2.038(07)	0.0449	1.764(08)
4	1.591(−09)	1.0274	1.196(01)	2.038(07)	0.0449	1.764(08)
5	4.803(−11)	0.3781	1.920(04)	4.025(07)	0.5220	5.410(03)

The difference in RR rate coefficients is much less pronounced, at all temperatures. At low temperatures, the stability against autoionization for all n distinguishes RR of the ground level. There is little difference for metastables levels of the excited term because the highest stable recombined n is (almost) independent of the fine-structure parent.

In tables 5 and 6, we present separately the fitting coefficients for our total DR and RR rate coefficients for the ground and metastable levels (indexed by m), which are based upon the functional forms given by equations (16) and (17), respectively. The fits are accurate to better than 1% over $z^2(10^1$–$10^7)$ K, where $z = 13$ here.

6. Summary

We have carried-out a series of multi-configuration Breit–Pauli calculations for the dielectronic recombination of Fe^{13+}. Whilst there is much agreement between the theoretical velocity-convoluted cross sections and those determined experimentally by Schmidt *et al* (2006), differences over 0.1–10 eV lead to the experimentally-based total Maxwellian recombination rate coefficient being upwards of 50% larger than the theoretical one over the temperature range 10^4–10^5 K, which is typical of photoionized plasmas where Fe^{13+} is abundant. Such a difference lies well outside of the theoretical uncertainty, based-upon the accuracy of the radiative rates and sensitivity to resonance positions. It is also well outside of the experimental uncertainty of ±18% (Schmidt *et al* 2006).

It is difficult to see how to resolve this difference. Simply carrying-out a larger (configuration interaction) calculation would not be expected to result in a change much

beyond the difference, already noted, between the basis A and basis B results, especially given the level of agreement for radiative rates which we have observed between bases A and B and the extended basis 2 of Storey *et al* (1996). Furthermore, the good agreement between theory and experiment at higher $\Delta n = 0$ energies is interrupted twice by disconcerting differences spanning several electron volts. Such differences are also outside of the range of higher-order effects such as interacting resonances and the interference between DR and RR. Perhaps the results of a separate, independent, calculation will shed some light on the matter.

Nevertheless, the theoretical recombination rate coefficient determined here for Fe^{13+} is an order of magnitude larger than has been used by modellers in the past at photoionized plasma temperatures. This may help explain the discrepancy between the iron M-shell ionization balance predicted by photoionization modelling codes and that deduced from the iron M-shell unresolved-transition-array absorption feature observed in the x-ray spectra of many active galactic nuclei.

New data are clearly required for the other Fe $3p^q$ ions, especially $q = 2$–6, in order to eliminate the uncertainty in the DR atomic data used by CLOUDY, ION and XSTAR and to enable them to focus on the 'bigger picture'. Such work has been undertaken recently (Badnell 2006b) and similar results have been obtained as seen here for Fe^{13+}. This in turn demonstrates the need for similar multi-configuration Breit–Pauli calculations for other M-shell ions of astrophysical interest, e.g. Si, S, Ar, Ni, as well as a move into the 3d sub-shell of lower-charge Fe ions.

Acknowledgments

I would like to thank Eike Schmidt for supplying the experimental results in numerical form, Stefan Schippers for providing the survival probabilities applicable to the experimental set-up and Daniel Savin for commenting on an early draft of the manuscript. This work was supported, in part, by PPARC grant no. PPA\G\S2003\00055 with the University of Strathclyde.

References

Arnaud M and Raymond J 1992 *Astrophys. J.* **398** 394–406
Badnell N R 1987 *J. Phys. B: At. Mol. Phys.* **19** 3827–35
Badnell N R 1997 *J. Phys. B: At. Mol. Opt. Phys.* **30** 1–11
Badnell N R 2006a *Astrophys. J. Suppl. Ser.* at press (*Preprint* astro-ph/0604144)
Badnell N R 2006b *Astrophys. J. Lett.* **651** L73 (*Preprint* astro-ph/0608339)
Badnell N R, O'Mullane M G, Summers H P, Altun Z, Bautista M A, Colgan J, Gorczyca T W, Mitnik D M, Pindzola M S and Zatsarinny O 2003 *Astron. Astrophys.* **409** 1151–65
Badnell N R and Pindzola M S 1992 *Phys. Rev.* A **45** 2820–4
Badnell N R and Seaton M J 2003 *J. Phys. B: At. Mol. Opt. Phys.* **36** 4367–85
Behar E, Jacobs V L, Oreg J, Bar-Shalom A and Haan S L 2000 *Phys. Rev.* A **62** R030501(4)
Bethe H A and Salpeter E E 1957 *Quantum Mechanics of One- and Two-Electron Atoms* (Berlin: Springer)
Bryans P, Badnell N R, Gorczyca T W, Laming J M, Mitthumsiri W and Savin D W 2006 *Astrophys. J. Suppl. Ser.* at press (*Preprint* astro-ph/0604363)
Burgess A 1964 *Astrophys. J.* **139** 776–80
Burgess A, Mason H E and Tully J A 1989 *Astron. Astrophys.* **217** 319–28
Damburg R J and Kolosov V V 1979 *J. Phys. B: At. Mol. Phys.* **12** 2637–43
Dittner P F, Datz S, Miller P D and Pepmiller P L 1986 *Phys. Rev.* A **33** 124–30
Ferland G J 2006 Private communication, to be submitted
Fogle M, Badnell N R, Eklöw N, Mohamed T and Schuch R 2003 *Astron. Astrophys.* **409** 781–6
Fogle M, Badnell N R, Glans P, Loch S D, Madzunkov S, Abdel-Naby Sh A, Pindzola M S and Schuch R 2005 *Astron. Astrophys.* **442** 757–66
Gorczyca T W, Badnell N R and Savin D W 2002 *Phys. Rev.* A **65** 062707(8)
Gu M F 2003 *Astrophys. J.* **590** 1131–40

Jacobs V L, Davis J, Kepple P C and Blaha M 1977 *Astrophys. J.* **211** 605–11
Kallman T and Bautista M B 2001 *Astrophys. J. Suppl. Ser.* **133** 221–53
Kraemer S B, Ferland G J and Gabel J R 2004 *Astrophys. J.* **604** 556–61
Linkemann J *et al* 1995 *Nucl. Instrum. Methods Phys. Res.* B **98** 154–7
Mazzotta P, Mazzitelli G, Colafrancesco S and Vittorio N 1998 *Astron. Astrophys. Suppl. Ser.* **133** 403–9
Müller A 1999 *Int. J. Mass Spectrom.* **192** 9–22
Nahar S N 2000 *Astrophys. J. Suppl. Ser.* **126** 537–50
Netzer H 2004 *Astrophys. J.* **604** 551–5
Netzer H *et al* 2003 *Astrophys. J.* **599** 933–48
NIST Atomic Spectra Database v3.0.3 2006 http://physics.nist.gov/PhysRefData/ASD
Pindzola M S, Badnell N R and Griffin D C 1992 *Phys. Rev.* A **46** 5725–29
Savin D W *et al* 1997 *Astrophys. J.* **489** L115–8
Savin D W *et al* 2006 *Astrophys. J.* **642** 1275–85
Schippers S, Müller A, Gwinner G, Linkemann J, Saghiri A A and Wolf A 2001 *Astrophys. J.* **555** 1027–37
Schmidt E W *et al* 2006 *Astrophys. J.* **641** L157–60
Storey P J, Mason H E and Saraph H E 1996 *Astron. Astrophys.* **309** 677–82
Storey P J, Mason H E and Young P R 2000 *Astron. Astrophys. Suppl. Ser.* **141** 285–96
Verner D A and Ferland G J 1999 *Astrophys. J. Suppl. Ser.* **103** 467–73
Zong W, Schuch R, Gao H, DeWitt D R and Badnell N R 1998 *J. Phys. B: At. Mol. Opt. Phys.* **31** 3729–42